A Priori Analysis of Subgrid-Scale Models for Large Eddy Simulations of Supercritical Binary-Species Mixing Layers

Nora Okong'o* and Josette Bellan†
Jet Propulsion Laboratory
California Institute of Technology
Pasadena CA 91109-8099

Models for large eddy simulation (LES) are assessed on a database obtained from direct numerical simulations (DNS) of supercritical binary-species temporal mixing layers. The analysis is performed at the DNS transitional states for heptane/nitrogen, oxygen/hydrogen and oxygen/helium mixing layers. The incorporation of simplifying assumptions that are validated on the DNS database leads to a set of LES equations that requires only models for the subgrid scale (SGS) fluxes, which arise from filtering the convective terms in the DNS equations. Constant-coefficient versions of three different models for the SGS fluxes are assessed and calibrated. The Smagorinsky SGS-flux model shows poor correlations with the SGS fluxes, while the Gradient and Similarity models have high correlations, as well as good quantitative agreement with the SGS fluxes when the calibrated coefficients are used.

Introduction

Supercritical fluids are of great interest in extraction processes as well as in propulsion devices such as advanced gas-turbine and diesel engines, and liquid rockets. The performance of these devices depends on the efficiency of fluid disintegration and turbulent mixing, which may occur under supercritical conditions. A fluid is here defined to be in a supercritical state when it is at a thermodynamic pressure, p, or temperature, T, exceeding its critical (subscript c) value,[1] p_c or T_c; therefore, in the supercritical regime there is no longer the possibility of a two phase (i.e. gas/liquid) region.[2] For mixtures, both p_c and T_c depend on the composition. The present interest is in fluid mixtures at high pressures that are supercritical for the pure species. Past the critical point of the fluid (where material surfaces no longer exist), the disintegration of fluid jets displays an aspect that Chehroudi et al.[3] call 'fingers', or 'comb-like structures' at transcritical conditions, which have an increasingly gaseous appearance with increasing p. Similar experimental evidence was produced by Mayer et al.[4,5] for O_2 disintegration. For supercritical free N_2 jets, the experiments of Oschwald and Schik[6] also showed sharp density profiles, indicating the occurrence of sharp density gradients.

Results from Direct Numerical Simulations (DNS) showed, as in the experiments, that regions of high density-gradient-magnitude exist in both pre-transitional[7] and transitional[8,9] temporal mixing layers, arising both from the initial density stratification as well as from mixing.[10] These DNS were conducted using real-gas equations of state for non-ideal mixtures in conjunction with realistic transport properties and thermal

*Scientist, AIAA Member.
†Senior Research Scientist, AIAA Associate Fellow (corresponding author, josette.bellan@jpl.nasa.gov).

diffusion (Soret and Dufour) effects. For modeling fully turbulent supercritical flows at high pressures, Large Eddy Simulation (LES), wherein only the large-scales are simulated and the subgrid scales (SGS) are modeled, presently seems more computationally achievable for practical systems than DNS, which requires all turbulence scales to be resolved. The LES equations are derived by applying a spatial filter to the DNS equations, leading to various unclosed terms, including the SGS fluxes, which arise from filtering the convective terms. Given the distinctive supercritical flow characteristics, it is of interest to inquire whether LES models developed for compressible perfect-gas and incompressible flows can be extended to real-gas non-ideal mixtures.

In this paper, DNS databases for transitional supercritical temporal mixing layers[8,9] are analyzed on an *a priori* basis. In Section I, the LES governing equations are presented, in order to derive the unclosed terms that need to be modeled. Section II summarizes the DNS database, followed by the *a priori* analysis of the database in Section III. The analysis includes explicit modeling for the SGS fluxes and simplifying assumptions for the remaining unclosed terms. Finally, Section IV contains the conclusions and areas for future work.

I. Governing Equations for Large Eddy Simulations

The LES equations are derived from the DNS set by spatial filtering. The filtering operation is defined as:

$$\overline{\psi}(\vec{x}) = \int_V \psi(\vec{y}) G(\vec{x} - \vec{y}) d\vec{y} \tag{1}$$

where G is the filter function and V is the filtering volume; G has the property that for a spatially constant function, the filtered function is identical to the unfiltered one. For compressible flow, we use Favre filtering, defined as $\tilde{\psi} = \overline{\rho\psi}/\bar{\rho}$ where ρ is the density. The governing equations are written for the conservative variables $\phi = \{\rho, \rho u_i, \rho e_t, \rho Y_\alpha\}$ where u_i is the velocity component in the x_i-direction, e_t is the total energy and Y_α is the mass fraction for species α.

A. DNS Equations

The conservation equations for a mixture of N species are:

$$\frac{\partial \rho}{\partial t} + \frac{\partial \rho u_j}{\partial x_j} = 0 \tag{2}$$

$$\frac{\partial \rho u_i}{\partial t} + \frac{\partial \rho u_i u_j}{\partial x_j} = -\frac{\partial p}{\partial x_i} + \frac{\partial \sigma_{ij}}{\partial x_j} \tag{3}$$

$$\frac{\partial \rho e_t}{\partial t} + \frac{\partial \rho e_t u_j}{\partial x_j} = -\frac{\partial p u_j}{\partial x_j} - \frac{\partial q_j}{\partial x_j} + \frac{\partial \sigma_{ij} u_i}{\partial x_j} \tag{4}$$

$$\frac{\partial \rho Y_\alpha}{\partial t} + \frac{\partial \rho Y_\alpha u_j}{\partial x_j} = -\frac{\partial J_{\alpha j}}{\partial x_j} - w_\alpha \tag{5}$$

where t is the time, $\boldsymbol{\sigma}$ is the viscous stress tensor, $\mathbf{q}$ is the heat flux, $e = e_t - e_k$ is the internal energy, $e_k = u_i u_i/2$ is the kinetic energy, and $\mathbf{J}_\alpha$ and w_α are the species-mass flux and reaction rate of species α, respectively. Also,

$$\sum_{\alpha=1}^{N} Y_\alpha = 1, \quad \sum_{\alpha=1}^{N} J_{\alpha j} = 0, \quad \sum_{\alpha=1}^{N} w_\alpha = 0 \tag{6}$$

In this paper, the Einstein summation is used for roman indices (i, j, k), but not for Greek indices (α, β). The thermodynamic variables are functions of the flow field ϕ:

$$e = e(\phi), \quad p = p(\phi), \quad T = T(\phi), \quad h = h(\phi)$$

where p, T and the enthalpy h are computed from the equation of state (EOS); likewise, the transport quantities are functions of ϕ:

$$\sigma_{ij} = \sigma_{ij}(\phi), \quad J_{\alpha j} = J_{\alpha j}(\phi), \quad q_j = q_j(\phi)$$

For a Newtonian fluid,

$$\sigma_{ij} = \mu\left(\frac{\partial u_i}{\partial x_j} + \frac{\partial u_j}{\partial x_i} - \frac{2}{3}\frac{\partial u_k}{\partial x_k}\delta_{ij}\right) \tag{7}$$

where μ is the viscosity and S_{ij} is the rate-of-strain tensor.

The species-mass and heat fluxes originate in Keizer's[11] fluctuation-dissipation theory which is consistent with non-equilibrium thermodynamics, converges to kinetic theory in the low-pressure limit and relates fluxes and forces from first principles. The species-mass and heat fluxes take the form, including Soret and Dufour effects:[12]

$$J_{\alpha j} = -\sum_{\beta=1}^{N} \Lambda_{\alpha\beta j} \tag{8}$$

$$q_j = -\lambda\frac{\partial T}{\partial x_j} - \frac{1}{2}R_u T\sum_{\beta=1}^{N}\sum_{\alpha=1}^{N}\alpha_{IK,\alpha\beta}\frac{m}{m_\alpha m_\beta}\Lambda_{\alpha\beta} \tag{9}$$

$$\Lambda_{\alpha\beta} = \frac{m_\alpha m_\beta}{m}\left(\frac{\rho}{R_u}D_{m,\alpha\beta}Y_\alpha Y_\beta\right)\left[\frac{m}{m_\beta m_\alpha}R_u\alpha_{IK,\alpha\beta}\frac{1}{T}\frac{\partial T}{\partial x_j} + \frac{1}{m_\alpha}\frac{\partial}{\partial x_j}\left(\frac{\mu_\alpha}{T}\right) - \frac{1}{m_\beta}\frac{\partial}{\partial x_j}\left(\frac{\mu_\beta}{T}\right)\right] \tag{10}$$

$$\frac{\partial}{\partial x_j}\left(\frac{\mu_\alpha}{T}\right) = -\frac{h_{,\alpha}}{T^2}\frac{\partial T}{\partial x_j} + \frac{v_{,\alpha}}{T}\frac{\partial p}{\partial x_j} + R_u\sum_{\substack{\beta=1\\ \beta\neq\alpha}}^{N}\frac{\alpha_{D\alpha\beta}}{X_\alpha}\frac{\partial X_\beta}{\partial x_j} \tag{11}$$

$$\alpha_{D\alpha\beta} \equiv \frac{1}{R_u T}X_\alpha\frac{\partial\mu_\alpha}{\partial X_\beta} = \frac{\partial X_\alpha}{\partial X_\beta} + X_\alpha\frac{\partial \ln\gamma_\alpha}{\partial X_\beta} \tag{12}$$

For the mixture, λ is the thermal conductivity, R_u is the universal gas constant, m is the mixture molar mass, with the molar volume being $v = m/\rho$. For the pure species α, m_α is the species-α molar mass, μ_α is the chemical potential, $h_{,\alpha}$ is the partial molar enthalpy, $v_{,\alpha}$ is the partial molar volume, $X_\alpha = mY_\alpha/m_\alpha$ is the mole fraction, and γ_α is the fugacity. For the species-α/species-β pair, $\mathbf{\Lambda}_{\alpha\beta}$ is the binary species-mass flux ($\mathbf{\Lambda}_{\alpha\beta} = -\mathbf{\Lambda}_{\beta\alpha}$, $\mathbf{\Lambda}_{\alpha\alpha} = 0$), $\alpha_{IK,\alpha\beta}$ is the Irwing-Kirwood (IK) form of the thermal diffusion factor ($\alpha_{IK,\alpha\beta} = -\alpha_{IK,\beta\alpha}, \alpha_{IK,\alpha\alpha} = 0$), $D_{m,\alpha\beta}$ is the binary diffusion coefficient ($D_{m,\alpha\beta} = D_{m,\beta\alpha}$, $D_{m,\alpha\alpha} = 0$) and $\alpha_{D\alpha\beta}$ is the mass diffusion factor.

B. LES Equations

After filtering, and assuming that filtering and differentiation commute (true except near boundaries, where the filter function changes), the governing equations become:

$$\frac{\partial\bar{\rho}}{\partial t} + \frac{\partial\bar{\rho}\tilde{u}_j}{\partial x_j} = 0 \tag{13}$$

$$\frac{\partial\bar{\rho}\tilde{u}_i}{\partial t} + \frac{\partial\overline{\rho u_i u_j}}{\partial x_j} = -\frac{\partial\bar{p}}{\partial x_i} + \frac{\partial\bar{\sigma}_{ij}}{\partial x_j} \tag{14}$$

$$\frac{\partial\bar{\rho}\tilde{e}_t}{\partial t} + \frac{\partial\overline{\rho e_t u_j}}{\partial x_j} = -\frac{\partial\overline{pu_j}}{\partial x_j} - \frac{\partial\bar{q}_j}{\partial x_j} + \frac{\partial\overline{\sigma_{ij}u_i}}{\partial x_j} \tag{15}$$

$$\frac{\partial\bar{\rho}\tilde{Y}_\alpha}{\partial t} + \frac{\partial\overline{\rho Y_\alpha u_j}}{\partial x_j} = -\frac{\partial\bar{J}_{\alpha j}}{\partial x_j} - \bar{w}_\alpha \tag{16}$$

$$\tilde{e}_t = \tilde{e} + \widetilde{u_i u_i}/2, \ \sum_{\alpha=1}^{N} \tilde{Y}_{\alpha j} = 1, \ \sum_{\alpha=1}^{N} \bar{J}_{\alpha j} = 0, \ \sum_{\alpha=1}^{N} \bar{w}_\alpha = 0 \tag{17}$$

Using the previously adopted notation of denoting the DNS flow field as ϕ, the filtered flow field can now be denoted as $\overline{\phi}$ and we can define functions of the filtered flow field:

$$e\left(\overline{\phi}\right), \quad p\left(\overline{\phi}\right), \quad T\left(\overline{\phi}\right), \quad h\left(\overline{\phi}\right), \quad \sigma_{ij}\left(\overline{\phi}\right), \quad J_{\alpha j}\left(\overline{\phi}\right), \quad q_j\left(\overline{\phi}\right)$$

which have the same functional form as in the DNS and that in general differ from their filtered counterparts

$$\tilde{e} = \overline{\rho e\left(\overline{\phi}\right)}/\bar{\rho}, \ \bar{p} = \overline{p\left(\overline{\phi}\right)}, \ \bar{T} = \overline{T\left(\overline{\phi}\right)}, \ \tilde{T} = \overline{\rho T\left(\overline{\phi}\right)}/\bar{\rho}, \ \tilde{h} = \overline{\rho h\left(\overline{\phi}\right)}/\bar{\rho}, \ \bar{\sigma}_{ij} = \overline{\sigma_{ij}\left(\overline{\phi}\right)}, \ \bar{J}_{\alpha j} = \overline{J_{\alpha j}\left(\overline{\phi}\right)}, \ \bar{q}_j = \overline{q_j\left(\overline{\phi}\right)}$$

Defining the SGS fluxes,

$$\tau_{ij} = \widetilde{u_i u_j} - \tilde{u}_i \tilde{u}_j, \quad \zeta_j = \widetilde{h u_j} - \tilde{h}\tilde{u}_j, \quad \eta_{\alpha j} = \widetilde{Y_\alpha u_j} - \tilde{Y}_\alpha \tilde{u}_j \text{ with } \sum_{\alpha=1}^{N} \eta_{\alpha j} = 0 \tag{18}$$

the filtered governing equations are:

$$\frac{\partial \bar{\rho}}{\partial t} + \frac{\partial \bar{\rho}\tilde{u}_j}{\partial x_j} = 0 \tag{19}$$

$$\frac{\partial \bar{\rho}\tilde{u}_i}{\partial t} + \frac{\partial \bar{\rho}\tilde{u}_i\tilde{u}_j}{\partial x_j} = -\frac{\partial p\left(\overline{\phi}\right)}{\partial x_i} + \frac{\partial \sigma_{ij}\left(\overline{\phi}\right)}{\partial x_j} - \frac{\partial}{\partial x_j}\left(\bar{\rho}\tau_{ij}\right) - \frac{\partial}{\partial x_i}\left[\bar{p} - p\left(\overline{\phi}\right)\right] + \frac{\partial}{\partial x_j}\left[\bar{\sigma}_{ij} - \sigma_{ij}\left(\overline{\phi}\right)\right] \tag{20}$$

$$\begin{aligned}\frac{\partial \bar{\rho}\tilde{e}_t}{\partial t} + \frac{\partial \bar{\rho}\tilde{e}_t\tilde{u}_j}{\partial x_j} = &-\frac{\partial p\left(\overline{\phi}\right)\tilde{u}_j}{\partial x_j} - \frac{\partial q_j\left(\overline{\phi}\right)}{\partial x_j} + \frac{\partial \sigma_{ij}\left(\overline{\phi}\right)\tilde{u}_i}{\partial x_j} - \frac{\partial}{\partial x_j}\left(\bar{\rho}\zeta_j\right) - \frac{\partial}{\partial x_j}\left(\bar{\rho}\kappa_j\right) \\ &- \frac{\partial}{\partial x_j}\left\{\left[\bar{p} - p\left(\overline{\phi}\right)\right]\tilde{u}_j\right\} - \frac{\partial}{\partial x_j}\left[\bar{q}_j - q_j\left(\overline{\phi}\right)\right] + \frac{\partial}{\partial x_j}\left[\overline{\sigma_{ij}u_i} - \sigma_{ij}\left(\overline{\phi}\right)\tilde{u}_i\right]\end{aligned} \tag{21}$$

$$\frac{\partial \bar{\rho}\tilde{Y}_\alpha}{\partial t} + \frac{\partial \bar{\rho}\tilde{Y}_\alpha\tilde{u}_j}{\partial x_j} = -\frac{\partial J_{\alpha j}\left(\overline{\phi}\right)}{\partial x_j} - \bar{w}_\alpha - \frac{\partial}{\partial x_j}\left(\bar{\rho}\eta_{\alpha j}\right) - \frac{\partial}{\partial x_j}\left[\bar{J}_{\alpha j} - J_{\alpha j}\left(\overline{\phi}\right)\right] \tag{22}$$

where $\kappa_j = \widetilde{e_k u_j} - \tilde{e}_k\tilde{u}_j$. These equations contain several unclosed terms that cannot be directly computed from the filtered flow field. To compute these terms, we pursue two closure approaches: explicit models for the SGS fluxes, and simplifying assumptions for the remaining terms. The assumptions and models will be assessed in Section III on a DNS database, described below, of a binary non-reacting temporal mixing layer.

II. Description of DNS database

The database consists of supercritical temporal mixing layer simulations of binary ($N = 2$) mixtures, namely, heptane/nitrogen (HN), oxygen/hydrogen (OH) and oxygen/helium (OHe). The pure species properties are listed in Table 1. For each layer, the lighter molar mass species is indexed as species 1 while the heavier molar mass species is indexed as species 2; the notation is simplified as $D \equiv D_{21}$, $\alpha_{IK} \equiv \alpha_{IK,21}$, $\alpha_D \equiv \alpha_{D,21}$, $\eta_j \equiv \eta_{2j}$. The flows are non-reacting, i.e. $w_\alpha \equiv 0$.

Table 1. Pure species properties.

Species	m (g/mol)	T_c (K)	p_c(MPa)
H_2	2.016	33.0	1.284
He	4.003	5.19	0.227
N_2	28.013	126.3	3.399
O_2	31.999	154.6	5.043
C_7H_{16}	100.205	540.2	2.74

A detailed description of the DNS methodology has been given by Miller et al.[7] and Okong'o and Bellan[8] for C_7H_{16}/N_2 layers and by Okong'o et al.[9] for

the O_2/H_2 layers. The conservation equations were numerically solved using a fourth-order explicit Runge-Kutta time integration and a sixth-order compact scheme with eighth-order filter for spatial derivatives;[20] the filtering is required to maintain numerical stability for long-time integrations and is applied at interior points only. The computations were parallelized using three-dimensional domain decomposition and message passing, and an efficient parallel tridiagonal solver.[21] The configuration, initial and boundary conditions, EOS, and transport property relations are summarized below.

A. Configuration, initial and boundary conditions

The temporally developing mixing layer configuration is depicted in Figure 1 for heptane/nitrogen, as an example, showing the definition of the streamwise (x_1), cross-stream (x_2) and spanwise (x_3) coordinates. The layer is not symmetric in extent in the x_2 direction, to accommodate the larger layer growth in the lighter fluid side. The free-stream density (ρ_1 or ρ_2) is calculated for each pure species at its free-stream temperature (T_1 or T_2) and at the initial uniform pressure (p_0). The vorticity thickness is defined as $\delta_\omega(t) = \Delta U_0 / (\partial \langle u_1 \rangle / \partial x_2)_{max}$ where $\langle u_1 \rangle$ is the (x_1, x_3) planar average of the streamwise velocity, and $\Delta U_0 = U_1 - U_2$ is the velocity difference across the layer. The choice

$$U_1 = \frac{2M_{c,0}a_{s_1}}{\left[1+\left(\frac{a_{s_1}}{a_{s_2}}\right)\sqrt{\frac{\rho_1 Z_1}{\rho_2 Z_2}}\right]},\ U_2 = -\sqrt{\frac{\rho_1 Z_1}{\rho_2 Z_2}}U_1 \quad (23)$$

was made with the intent of keeping the ultimate vortex stationary in the computational domain,[7] although the relations of Papamoschou and Roshko[16]

$$U_1 = \frac{2M_{c,0}a_{s_1}}{\left[1+\left(\frac{a_{s_1}}{a_{s_2}}\right)\sqrt{\frac{\rho_1}{\rho_2}}\right]},\ U_2 = -\sqrt{\frac{\rho_1}{\rho_2}}U_1 \quad (24)$$

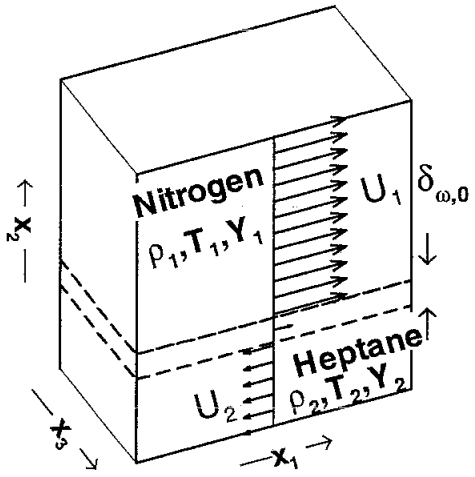

Figure 1. Sketch of the C7H16/N2 mixing layer configuration.

were also used for some simulations reported here. Here $M_{c,0}$ is the convective Mach number and $Z = p/(\rho T R_u/m)$ is the compression factor indicating departures from perfect gas ($Z = 1$) behavior. The specification of $M_{c,0}$ therefore determines ΔU_0. Given the initial streamwise velocity profile u_1 based on U_1 and U_2, $(\partial \langle u_1 \rangle / \partial x_2)_{max}$ and hence $\delta_{\omega,0} \equiv \delta_\omega(0)$ are calculated. The specified value of the initial flow Reynolds number, $\mathrm{Re}_0 = (1/2)(\rho_1 + \rho_2)\Delta U_0 \delta_{\omega,0}/\mu_R$, chosen so as to enable the resolution of all relevant length scales, is then used to calculate μ_R. The grid spacing is an approximately linear function of Re_0.

The simulations are started with error-function profiles for the mean streamwise velocity, mass fraction and temperature, upon which are imposed spanwise and streamwise vorticity perturbations[17,18] of strengths F_{2D} and F_{3D} respectively, whose streamwise (λ_1) and spanwise (λ_3) wavelengths are $\lambda_1 = C\delta_{\omega,0}$ and $\lambda_3 = 0.6\lambda_1$, where C=7.29 is the most unstable wavelength for incompressible flow. For the simulations reported here, listed in Table 2, other values of C obtained from stability analyses[9] were also used: C =4.57 for the shortest (estimated) unstable wavelength for the C_7H_{16}/N_2 layer, or C corresponding to the most unstable wavelength for O_2 layers. The grid is chosen for all simulations so as to accommodate four wavelengths in the streamwise and spanwise directions, and the evolution of the layer is meant to encompass roll-up and two pairings of the four initial spanwise vortices into an ultimate vortex.

The boundary conditions are periodic in the streamwise and spanwise directions, and of outflow type for real gas in the cross-stream direction, as derived by Okong'o and Bellan.[19] The outflow type conditions are

Table 2. Simulation parameters for supercritical temporal mixing layer database

Run	HN400	HN500	HN600	HN800	OH750	OH550	OH500	OHe600
Species 2	C_7H_{16}	C_7H_{16}	C_7H_{16}	C_7H_{16}	O_2	O_2	O_2	O_2
Species 1	N_2	N_2	N_2	N_2	H_2	H_2	H_2	He
T_2 (K)	600	600	600	600	400	400	235	235
T_1 (K)	1000	1000	1000	1000	600	600	287	287
ρ_2/ρ_1	12.88	12.88	12.88	12.88	24.40	24.40	24.51	12.17
p_0 (atm)	60	60	60	60	100	100	100	100
Re_0	400	500	600	800	750	550	500	600
$\lambda_1/\delta_{\omega,0}$	7.29	7.29	7.29	4.57	7.29	10.35	10.61	9.31
L_1 (m)	0.200	0.200	0.200	0.125	0.200	0.284	0.284	0.255
L_2 (m)	0.232	0.232	0.232	0.148	0.200	0.284	0.284	0.255
L_3 (m)	0.120	0.120	0.120	0.075	0.120	0.170	0.170	0.153
N_1	192	240	288	240	352	352	352	352
N_2	224	288	336	272	352	352	352	352
N_3	112	144	176	144	208	208	208	208
Δx (10^{-4}m)	10.71	8.36	6.97	5.23	5.77	8.19	8.39	7.36
F_{2D}	0.1	0.1	0.1	0.1	0.1	0.1	0.1	0.05
F_{3D}	0.05	0.05	0.05	0.05	0.05	0.025	0.025	0.0125
t^*_{trans}	150	155	135	100	150	270	290	220
$\mathrm{Re}_{m,trans}$	972	1250	1452	1258	1507	1907	1772	2004

All simulations have $M_{c,0}$=0.4, $L_1 = 4\lambda_1$ and $L_3 = 0.6L_1$. N_i is the number points in the x_i-direction, $\Delta x = \max\{\Delta x_1, \Delta x_2, \Delta x_3\}$.

essential to maintain numerical stability since the initial perturbation causes large pressure waves that must be allowed out of the domain with minimal reflection.

B. Equation of state

The pressure is calculated from the well-known Peng-Robinson (PR) EOS, given T and the PR molar volume (v_{PR}), as

$$p = \frac{R_u T}{(v_{PR} - b_m)} - \frac{a_m}{(v_{PR}^2 + 2b_m v_{PR} - b_m^2)}, \tag{25}$$

where a_m and b_m are functions of T and X_α. At high pressures, v_{PR} may differ significantly from the actual molar volume v.[1] Both v_{PR} and the volume shift ($v_S = v - v_{PR}$) can be calculated from the PR EOS given p, T and X_α,[13] although for the C_7H_{16}/N_2 system v_S is negligible. All thermodynamic quantities, including α_D, h, $C_p = (\partial h/\partial T)_{p,X}$ and the speed of sound (a_s), are calculated from the EOS using standard thermodynamic relations.[7,8,14] The implementation of the EOS to calculate p and T from ρ, e and Y_α uses an iterative scheme[14] for O_2/H_2 and O_2/He, and an energy fit[8] for C_7H_{16}/N_2.

C. Transport coefficients

The viscosity, the Schmidt number ($Sc = \mu/(\rho\alpha_D D)$) and the Prandtl number ($\mathrm{Pr} = \mu C_p/(m\lambda)$) were calculated from high-pressure single-species transport properties using mixing rules, as in Harstad and Bellan.[15] The calculated values were correlated, as summarized in Table 3, and these correlations are then used

Table 3. Transport properties for binary mixtures. $T_R = (T_1 + T_2)/2$, T in Kelvin.

System	C_7H_{16}/N_2	O_2/H_2	O_2/He
$\mu = \mu_R (T/T_R)^n$	$n = 0.7$	$n = 0.75$	$n = 0.59$
$Sc \equiv \mu/(\rho \alpha_D D)$	$1.5 - Y_2$	$\left[\left(1.334 - 0.668Y_2 - 0.186Y_2^2 - 0.268Y_2^6\right) \times \left[1 + (88.6/T)^{1.5}\right] \right]$	Eq. 41
$\Pr \equiv \mu C_p/(m\lambda)$	$0.5Sc/\exp(-1.5Y_2)$	$1.335/T^{0.1}$	Eq. 40
α_{IK} or α_{BK}	$\alpha_{IK} = 0.1$ (Ref. 12)	$\alpha_{BK} = 0.2$ (Refs. 15, 30)	$\alpha_{BK} = 0.25$
T Range	500K–1100K	200K–800K	100K–900K
p Range	40 atm–80 atm	~100atm	~100atm

to compute the transport properties μ, D and λ. One of the thermal diffusion factors is specified, then the other is calculated from

$$\alpha_{BK} = \alpha_{IK} - \frac{1}{R_u T} \frac{m_2 m_1}{m} \left(\frac{h_{,2}}{m_2} - \frac{h_{,1}}{m_1} \right) \tag{26}$$

where α_{BK} is the Bearman-Kirkwood (BK) form of the thermal diffusion factor.

III. Results

The database used for the *a priori* analysis is summarized in Table 2. Note that the grid spacing is uniform with $\Delta x_1 \simeq \Delta x_2 \simeq \Delta x_3$; we denote $\Delta x = \max\{\Delta x_i\}$. The flow fields are filtered using a cubic-top hat filter, for which the filtered value is simply the volume-average. The filter width used is $\bar{\Delta}$, with $\bar{\Delta}/\Delta x$=4 or 8. Further filtering is performed at the test-filter width $\hat{\Delta}$, with $\hat{\Delta}/\bar{\Delta}$=1 or 2. All calculations are performed on the DNS grid. The analysis is carried out at the transitional states listed in Table 2. The differing thermodynamics of the various species-systems preclude matching of the initial density stratification (ρ_2/ρ_1) or of the transitional momentum thickness[9,14] within the regimes of practical interest, since there is not a simple relationship between the initial conditions and the transitional state. As a result, the O_2 layers ended up with higher momentum-thickness Reynolds number, Re_m, at the transitional state, with the O_2/He layer having the highest value of 2004. While the HN layers have lower initial ρ_2/ρ_1, they have higher density gradient magnitude $|\nabla\rho|\,\delta_{\omega,0}/(\rho_2 - \rho_1)$ at the transitional state, due to their higher mixture non-ideality.[10] Since the appropriate LES resolution (Δx_{LES}) depends on the gradients of the filtered flow field, the implication is that HN LES may require higher resolution relative to DNS (i.e., less grid coarsening, smaller $\bar{\Delta}/\Delta x_{DNS}$ and $\Delta x_{LES}/\Delta x_{DNS}$) than LES for the other species systems considered.

A. LES assumptions

Following a protocol previously used for an atmospheric two-phase mixing layer,[22] we evaluate the following LES assumptions, with a view to simplifying Eqs. 20–22:

$$\tilde{e} = e\left(\widetilde{\phi}\right), \quad \overline{T} = T\left(\widetilde{\phi}\right), \quad \widetilde{T} = T\left(\widetilde{\phi}\right), \quad \bar{p} = p\left(\widetilde{\phi}\right), \quad \tilde{h} = h\left(\widetilde{\phi}\right) \tag{27}$$

$$\overline{\sigma}_{ij} = \sigma_{ij}\left(\widetilde{\phi}\right), \quad \bar{J}_{\alpha j} = J_{\alpha j}\left(\widetilde{\phi}\right), \quad \bar{q}_j = q_j\left(\widetilde{\phi}\right), \quad \overline{u_i \sigma_{ij}} = \widetilde{u}_i \sigma_{ij}\left(\widetilde{\phi}\right) \tag{28}$$

$$\bar{\rho}\kappa_j = \tfrac{1}{2}(\overline{\rho u_i u_i u_j} - \overline{\rho u_i u_i}\widetilde{u}_j) = \bar{\rho}\tau_{ij}\widetilde{u}_i \tag{29}$$

The LES assumptions tested are listed in Table 4, where the slopes from least-squares fit of the model (RHS) to the terms (LHS) are tabulated. Correlations between the models and terms (not shown) were excellent (typically above 98%), being somewhat lower for the larger filter width. Correspondingly, compared to the values at the smaller filter width, the slopes in Table 4 also show greater deviation from the ideal value

of unity at the larger filter width. The thermodynamic assumptions (Eq. 27) have less than 1% error on all the flow fields. The assumptions for the viscous, heat and species-mass fluxes are almost as accurate, with errors of about 4%. The model for the triple correlation (Eq. 29) appears to be the least accurate assumption, with errors of up to 10%. Therefore, it would appear that the filtered thermodynamic quantities (internal energy, temperature, pressure and enthalpy) and the filtered viscous, heat and species-mass fluxes can be adequately modeled from the filtered flow field. The same results were previously obtained in an atmospheric-pressure perfect-gas mixing layer,[22] although here the species-mass and heat fluxes have a much more complicated functional form (Eqs. 8 and 9), including Soret and Dufour (thermal diffusion) effects.

Incorporating the validated LES assumptions, Eqs. 19–22 become:

$$\frac{\partial \bar{\rho}}{\partial t} + \frac{\partial \bar{\rho}\tilde{u}_j}{\partial x_j} = 0 \tag{30}$$

$$\frac{\partial \bar{\rho}\tilde{u}_i}{\partial t} + \frac{\partial \bar{\rho}\tilde{u}_i\tilde{u}_j}{\partial x_j} = -\frac{\partial p\left(\bar{\phi}\right)}{\partial x_i} + \frac{\partial \sigma_{ij}\left(\bar{\phi}\right)}{\partial x_j} - \frac{\partial}{\partial x_j}\left(\bar{\rho}\tau_{ij}\right) \tag{31}$$

$$\frac{\partial \bar{\rho}\tilde{e}_t}{\partial t} + \frac{\partial \tilde{\rho}\tilde{e}_t\tilde{u}_j}{\partial x_j} = -\frac{\partial p\left(\bar{\phi}\right)\tilde{u}_j}{\partial x_j} - \frac{\partial q_j\left(\bar{\phi}\right)}{\partial x_j} + \frac{\partial \sigma_{ij}\left(\bar{\phi}\right)\tilde{u}_i}{\partial x_j} - \frac{\partial}{\partial x_j}\left(\bar{\rho}\zeta_j\right) - \frac{\partial}{\partial x_j}\left(\bar{\rho}\tau_{ij}\tilde{u}_i\right) \tag{32}$$

$$\frac{\partial \bar{\rho}\tilde{Y}_\alpha}{\partial t} + \frac{\partial \bar{\rho}\tilde{Y}_\alpha\tilde{u}_j}{\partial x_j} = -\frac{\partial J_{\alpha j}\left(\bar{\phi}\right)}{\partial x_j} - \bar{w}_\alpha - \frac{\partial}{\partial x_j}\left(\bar{\rho}\eta_{\alpha j}\right) \tag{33}$$

Eqs. 30–33 still contain unclosed terms, namely the SGS fluxes, that will be modeled explicitly.

B. SGS-flux models

The three basic models for the SGS fluxes (τ_{ij}, $\eta_{\alpha j}$, ζ_j) are[22] the Smagorinsky (SM) model, the Gradient (GR) model and the Scale-Similarity (SS) model. For the *a priori* analysis, only constant coefficient versions of these models can be considered, although dynamic-coefficient versions should also be studied in *a posteriori* LES.[23] Because dynamic models are based on the same concept as the SS model, the *a priori* evaluation of that model should provide reasonable indications of the likely performance of dynamic models. Although in this paper we will calibrate the constant-coefficients, it should be kept in mind that other effects that cannot be studied *a priori*, such as the interaction of the resolved flow with the SGS, may dictate a different value in actual LES. Note that the calibration will consider the same coefficient value for all SGS fluxes, although practical implementation may require different values for different fluxes, in addition to the spatial and temporal variation of coefficients that is afforded by dynamic modeling.[23]

The SM model, which is based on the gradient-diffusion (eddy-viscosity) concept, is[24]

$$\tau_{ij} - \frac{1}{3}\tau_{kk}\delta_{ij} = -C_{SM}\bar{\Delta}^2 S\left(\bar{\phi}\right)\left[S_{ij}\left(\bar{\phi}\right) - \frac{1}{3}S_{kk}\left(\bar{\phi}\right)\delta_{ij}\right] \tag{34}$$

$$\eta_{\alpha j} = -C_{SM}\bar{\Delta}^2 S\left(\bar{\phi}\right)\frac{1}{2}\frac{\partial \tilde{Y}_\alpha}{\partial x_j},\ \zeta_j = -C_{SM}\bar{\Delta}^2 S\left(\bar{\phi}\right)\frac{1}{2}\frac{\partial \tilde{h}}{\partial x_j} \tag{35}$$

where $S^2\left(\phi\right) = S_{mn}\left(\phi\right)S_{mn}\left(\phi\right)$. The Yoshizawa[25] (YO) model for τ_{kk} is

$$\tau_{kk} = C_{YO}\bar{\Delta}^2 S^2\left(\bar{\phi}\right) \tag{36}$$

The GR model, derived from a Taylor series expansion, is[26]

$$\tau_{ij} = C_{GR}\bar{\Delta}^2\frac{\partial \tilde{u}_i}{\partial x_k}\frac{\partial \tilde{u}_j}{\partial x_k},\ \zeta_j = C_{GR}\bar{\Delta}^2\frac{\partial \tilde{h}}{\partial x_k}\frac{\partial \tilde{u}_j}{\partial x_k},\ \eta_{\alpha j} = C_{GR}\bar{\Delta}^2\frac{\partial \tilde{Y}_\alpha}{\partial x_k}\frac{\partial \tilde{u}_j}{\partial x_k},\ \sigma^2_{SGS} = C_{GR}\bar{\Delta}^2\frac{\partial \tilde{\psi}}{\partial x_k}\frac{\partial \tilde{\psi}}{\partial x_k} \tag{37}$$

Table 4. Slopes from least squares fit of RHS/LHS. For quantities with more than one component, the slope listed is that with the largest deviation from unity.

Run	HN400	HN500	HN600	HN800	OH750	OH550	OH500	OHe600
t^*_{trans}	150	155	135	100	150	270	290	220
$\mathrm{Re}_{m,trans}$	972	1250	1452	1258	1507	1907	1772	2004
$\tilde{e} = e\left(\overline{\phi}\right)$ ($\bar{\Delta}/\Delta x$=4)	1.0001	1.0001	1.0001	1.0001	1.0000	1.0000	1.0000	1.0002
$\tilde{e} = e\left(\overline{\phi}\right)$ ($\bar{\Delta}/\Delta x$=8)	1.0002	1.0002	1.0002	1.0002	1.0001	1.0001	1.0001	1.0006
$\overline{T} = T\left(\overline{\phi}\right)$ ($\bar{\Delta}/\Delta x$=4)	0.9982	0.9989	0.9986	0.9983	0.9999	0.9999	0.9999	0.9999
$\overline{T} = T\left(\overline{\phi}\right)$ ($\bar{\Delta}/\Delta x$=8)	0.9949	0.9968	0.9961	0.9953	0.9998	0.9998	0.9999	0.9998
$\widetilde{T} = T\left(\widetilde{\phi}\right)$ ($\bar{\Delta}/\Delta x$=4)	0.9992	0.9947	0.9994	0.9993	1.0005	1.0006	1.0003	1.0005
$\widetilde{T} = T\left(\widetilde{\phi}\right)$ ($\bar{\Delta}/\Delta x$=8)	0.9977	0.9985	0.9983	0.9980	1.0015	1.0018	1.0009	1.0015
$\bar{p} = p\left(\overline{\phi}\right)$ ($\bar{\Delta}/\Delta x$=4)	0.9996	0.9998	0.9996	0.9996	1.0001	1.0001	1.0001	1.0002
$\bar{p} = p\left(\overline{\phi}\right)$ ($\bar{\Delta}/\Delta x$=8)	0.9987	0.9993	0.9987	0.9986	1.0003	1.0003	1.0003	1.0005
$\tilde{h} = h\left(\overline{\phi}\right)$ ($\bar{\Delta}/\Delta x$=4)	0.9999	1.0000	0.9999	0.9999	1.0000	1.0000	1.0000	1.0002
$\tilde{h} = h\left(\overline{\phi}\right)$ ($\bar{\Delta}/\Delta x$=8)	0.9998	0.9999	0.9998	0.9998	1.0001	1.0001	1.0001	1.0005
$\overline{\sigma}_{ij} = \sigma_{ij}\left(\overline{\phi}\right)$ ($\bar{\Delta}/\Delta x$=4)	0.9924	0.9969	0.9972	0.9912	1.0053	1.0038	0.9987	1.0171
$\overline{\sigma}_{ij} = \sigma_{ij}\left(\overline{\phi}\right)$ ($\bar{\Delta}/\Delta x$=8)	0.9764	0.9867	0.9853	0.9610	1.0095	1.0057	0.9935	1.0273
$\bar{J}_{\alpha j} = J_{\alpha j}\left(\overline{\phi}\right)$ ($\bar{\Delta}/\Delta x$=4)	1.0086	1.0080	1.0099	1.0111	1.0035	1.0046	1.0032	1.0018
$\bar{J}_{\alpha j} = J_{\alpha j}\left(\overline{\phi}\right)$ ($\bar{\Delta}/\Delta x$=8)	0.9709	0.9861	0.9886	0.9653	1.0046	1.0078	1.0045	0.9964
$\bar{q}_j = q_j\left(\overline{\phi}\right)$ ($\bar{\Delta}/\Delta x$=4)	1.0330	1.0253	1.0258	1.0456	1.0046	1.0053	1.0036	1.0027
$\bar{q}_j = q_j\left(\overline{\phi}\right)$ ($\bar{\Delta}/\Delta x$=8)	1.0389	1.0344	1.0326	1.0365	1.0067	1.0093	1.0052	0.9971
$\overline{u_i\sigma_{ij}} = \widetilde{u}_i\sigma_{ij}\left(\overline{\phi}\right)$ ($\bar{\Delta}/\Delta x$=4)	1.0196	0.9980	1.0070	1.0112	1.0131	1.0093	1.0063	1.0026
$\overline{u_i\sigma_{ij}} = \widetilde{u}_i\sigma_{ij}\left(\overline{\phi}\right)$ ($\bar{\Delta}/\Delta x$=8)	1.0235	0.9854	0.9787	0.9325	1.0217	1.0197	1.0132	0.9941
$\bar{\rho}\kappa_j = \bar{\rho}\tau_{ij}\widetilde{u}_i$ ($\bar{\Delta}/\Delta x$=4)	0.9788	1.0453	0.9818	0.9535	0.9859	0.9946	1.0054	1.0099
$\bar{\rho}\kappa_j = \bar{\rho}\tau_{ij}\widetilde{u}_i$ ($\bar{\Delta}/\Delta x$=8)	0.9611	1.0845	0.9658	0.9070	0.9682	0.9862	1.0156	1.0131

where the SGS standard deviation, σ_{SGS}, of a generic variable ψ is defined as

$$\sigma^2_{SGS}\left(\tilde{\psi}\right) = \widetilde{\psi\psi} - \tilde{\psi}\tilde{\psi}, \quad \sigma_{SGS}\left(\bar{\psi}\right) = \overline{\psi\psi} - \bar{\psi}\,\bar{\psi} \tag{38}$$

(Note: $\sigma_{SGS}\left(\tilde{u}_1\right) = \tau_{11}$, $\sigma_{SGS}\left(\tilde{u}_2\right) = \tau_{22}$, $\sigma_{SGS}\left(\tilde{u}_3\right) = \tau_{33}$.) Theoretically, C_{GR} is proportional to the moments of inertia of the filtering volume; for a cubic top-hat filter $C_{GR} = 1/12$.

The SS model, which postulates similarity between the SGS and the small resolved scale, is[27]

$$\tau_{ij} = C_{SS}\left(\widehat{\widetilde{u}_i\widetilde{u}_j} - \widehat{\widetilde{u}}_i\widehat{\widetilde{u}}_j\right),\ \zeta_j = C_{SS}\left(\widehat{\tilde{h}\widetilde{u}_j} - \widehat{\tilde{h}}\widehat{\widetilde{u}}_j\right),\ \eta_{\alpha j} = C_{SS}\left(\widehat{\tilde{Y}_\alpha\widetilde{u}_j} - \widehat{\tilde{Y}}_\alpha\widehat{\widetilde{u}}_j\right),\ \sigma^2_{SGS} = C_{SS}\left(\widehat{\tilde{\psi}\tilde{\psi}} - \widehat{\tilde{\psi}}\widehat{\tilde{\psi}}\right) \tag{39}$$

where the overhat ($\widehat{\ }$) denotes (unweighted) filtering at the test-filter level $\hat{\Delta}$. Two test filter widths are considered, leading to models SS1 ($\hat{\Delta}/\bar{\Delta} = 1$) and SS2 ($\hat{\Delta}/\bar{\Delta} = 2$). While scale-similarity would imply that $C_{SS} = 1$, the actual value is filter-width dependent.[22,28,29]

Least squares fits of the exact SGS fluxes to the SGS-flux models produced the slope (exact/model) and correlation for each SGS quantity; the model coefficient is the slope from the least squares fit. For each SGS model, the calibrated SGS coefficient for a given run and filter width is obtained by averaging the slopes obtained for each SGS quantity. The SM coefficient is based on 12 SGS quantities (6 independent τ_{ij}, 3 ζ_j, 3 η_j), whereas the GR and SS coefficients are based on an additional 6 SGS standard deviations. Due to the

Table 5. Slopes from least-squares fit of SGS models to SGS quantities (slope=exact/model), OHe600, $\bar{\Delta}/\Delta x$=8. The SM model τ_{ij} is compared to the exact $(\tau_{ij} - \tau_{kk}\delta_{ij}/3)$. For $\bar{\rho}\tau_{kk}$ using the YO model, the slope is 0.2275 and the correlation is 0.8332.

SGS quantity	SM	GR	SS $\left(\hat{\Delta}/\bar{\Delta}=1\right)$	SS $\left(\hat{\Delta}/\bar{\Delta}=2\right)$
$\bar{\rho}\tau_{11}$	0.0633	0.1269	1.4741	0.5141
$\bar{\rho}\tau_{22}$	0.0241	0.1241	1.5030	0.5667
$\bar{\rho}\tau_{33}$	0.0160	0.1210	1.4826	0.5574
$\bar{\rho}\tau_{12}$	0.0366	0.1133	1.3331	0.4572
$\bar{\rho}\tau_{13}$	0.0241	0.1158	1.4547	0.5348
$\bar{\rho}\tau_{23}$	0.0160	0.1143	1.5005	0.6108
$\bar{\rho}\zeta_1$	0.1662	0.1200	1.4647	0.5132
$\bar{\rho}\zeta_2$	0.0607	0.1143	1.4389	0.4802
$\bar{\rho}\zeta_3$	0.0522	0.1119	1.4371	0.4812
$\bar{\rho}\eta_1$	0.1683	0.1201	1.4641	0.5132
$\bar{\rho}\eta_2$	0.0591	0.1145	1.4378	0.4805
$\bar{\rho}\eta_3$	0.0509	0.1122	1.4360	0.4810
$\sigma^2_{SGS}(\tilde{u}_1)$	-	0.1200	1.4174	0.5088
$\sigma^2_{SGS}(\tilde{u}_2)$	-	0.1213	1.4535	0.5516
$\sigma^2_{SGS}(\tilde{u}_3)$	-	0.1190	1.4596	0.5602
$\sigma^2_{SGS}\left(\tilde{T}\right)$	-	0.1204	1.7133	0.7200
$\sigma^2_{SGS}\left(\tilde{Y}_2\right)$	-	0.1136	1.5360	0.6143
$\sigma^2_{SGS}(\tilde{p})$	-	0.1224	1.4021	0.5197
Average slope	0.0622	0.1180	1.4671	0.5369
Std. dev. of slopes	0.0577	0.0044	0.0230	0.0636
Average correlation	0.2313	0.9602	0.9492	0.8322

strong density variation, the actual calibration is performed for the product of density and SGS flux, that appears in Eqs. 31–33. The slopes and the average of the correlations are listed for OHe600 in Table 5. The correlations for the SS and GR models are typically better than 95% (better than 80% for SS2), whereas the correlations for the SM model are at best 50% and are typically about 20%. Whereas the GR and SS slopes have a narrow distribution, as indicated by their small standard deviation of the slopes, there is wide variation among SM slopes, with the standard deviation of the SM slopes being comparable in magnitude to the average. These characteristics of OHe600 are typical of all layers at both filter widths.

Figures 2 and 3 compare the different SGS-flux models in terms of their averages in homogeneous (x_1, x_3) planes for OHe600. The calibrated coefficient values (that is, the average slopes) from Table 5 are used for the comparison. The Smagorinsky model has poor agreement with the exact (computed) SGS fluxes for all components, consistent with the low correlations; its deficiencies cannot be remedied by simply using different coefficient values for the different types of fluxes. However, the Yoshizawa model correlates quite well (over 80%) with τ_{kk}, and in this case, where τ_{kk} dominates in τ_{ij}, the combination with the Smagorinsky model yields good predictions of τ_{11}, τ_{22}, and τ_{33}. In marked contrast to the Smagorinsky model, the Similarity and Gradient models clearly have both qualitative and quantitatively good agreement with the exact SGS fluxes for all components.

The calibrated coefficients for all layers in Table 2 are tabulated in Table 6. The calibrated coefficients are here compared to determine possible statistical equality of the values (based on t-tests with 5% confidence

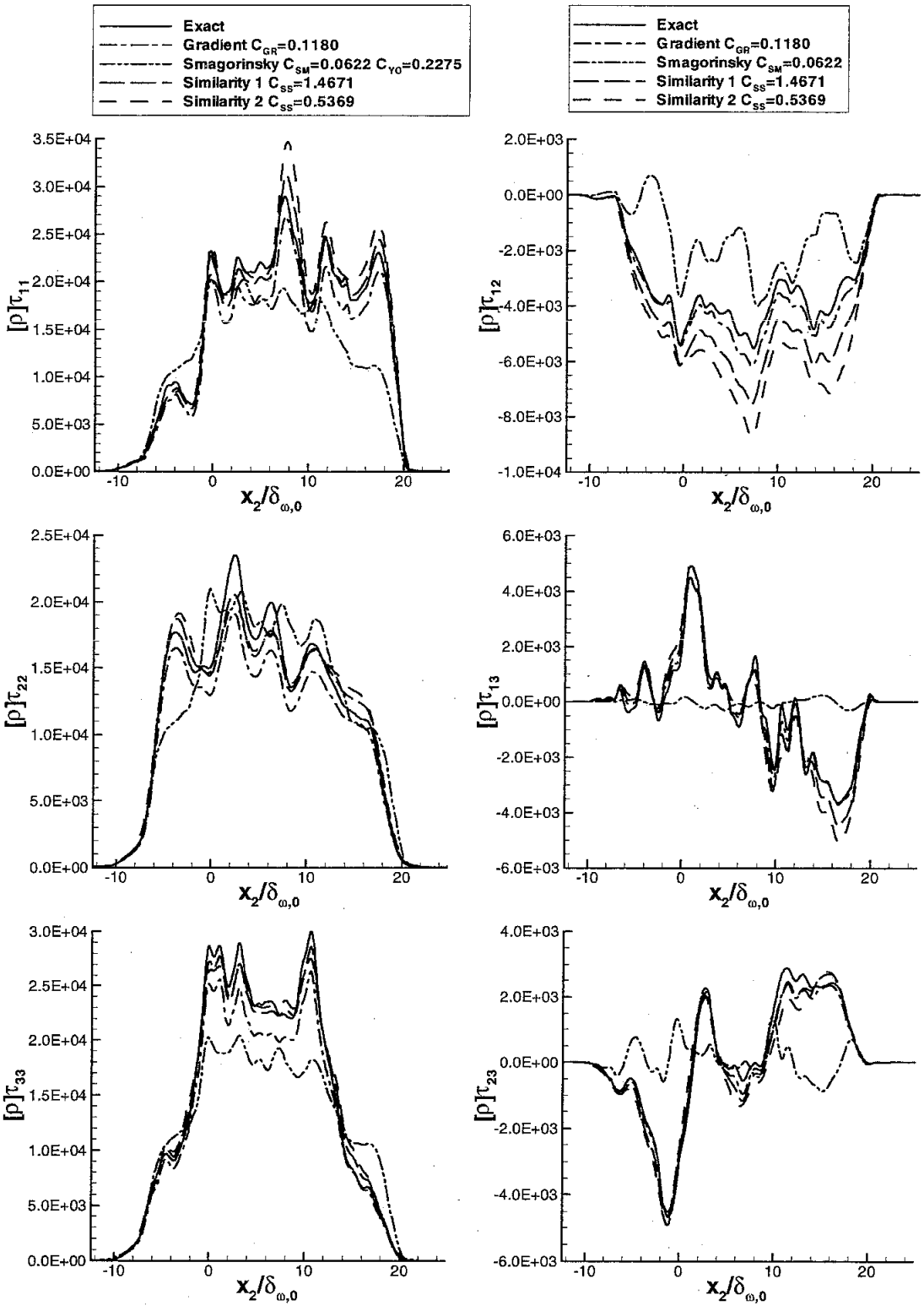

Figure 2. SGS fluxes and models for OHe600 with $\bar{\Delta}/\Delta x$=8, averages in homogeneous planes. ($[\rho] \equiv \bar{\rho}$.)

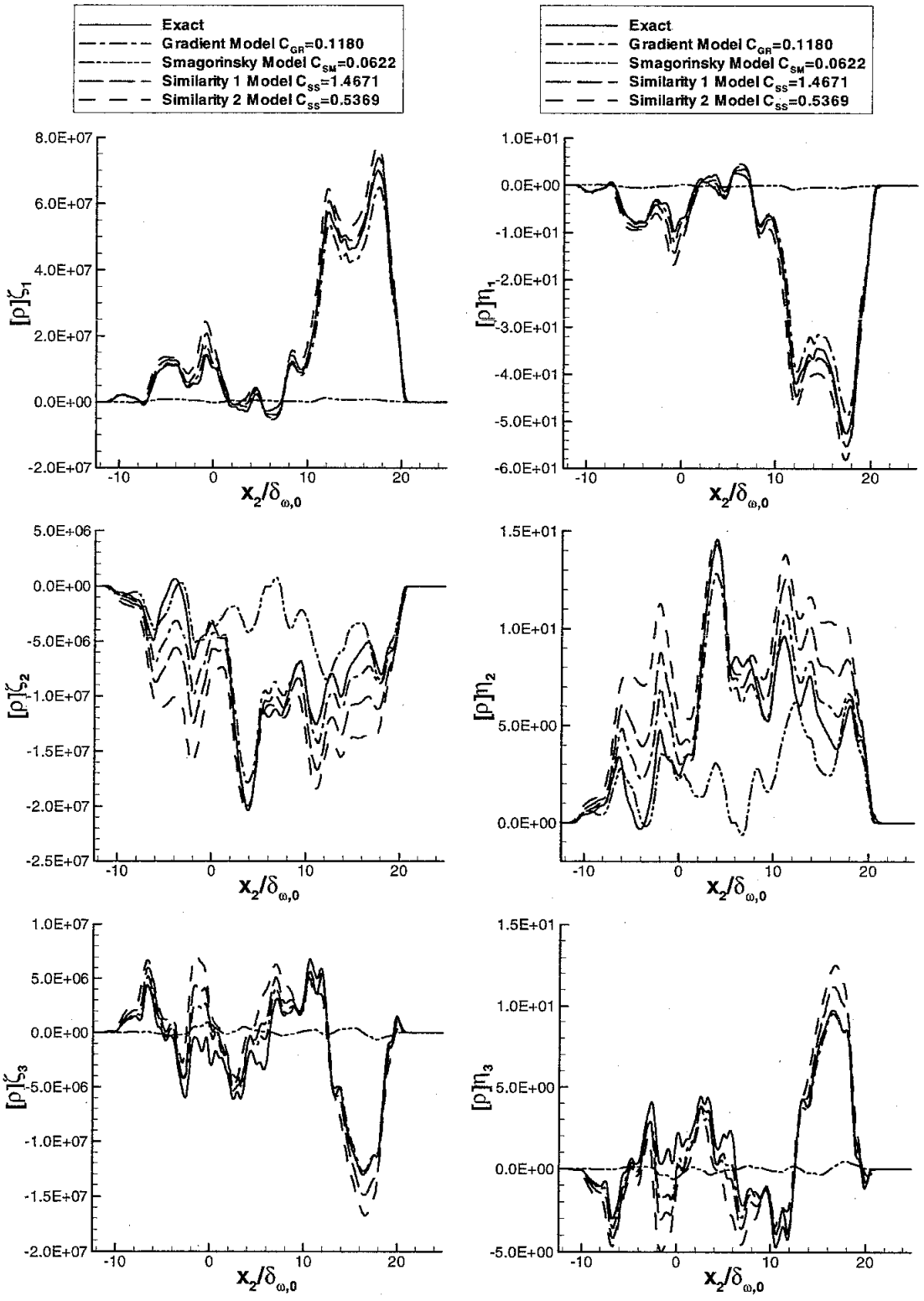

Figure 3. SGS fluxes and models for OHe600 with $\bar{\Delta}/\Delta x$=8, averages in homogeneous planes. ($[\rho] \equiv \bar{\rho}$.)

Table 6. Model cofficients calibrated from transitional states

Run	HN400	HN500	HN600	HN800	OH750	OH550	OH500	OHe600
t^*_{trans}	150	155	135	100	150	270	290	220
$\mathrm{Re}_{m,trans}$	972	1250	1452	1258	1507	1907	1772	2004
$C_{YO}\left(\frac{\bar{\Delta}}{\Delta x}=4\right)$	0.2751	0.2687	0.2583	0.2612	0.2396	0.2383	0.2398	0.2477
$C_{YO}\left(\frac{\bar{\Delta}}{\Delta x}=8\right)$	0.2751	0.2634	0.2471	0.2506	0.2144	0.2150	0.2137	0.2275
$C_{SM}\left(\frac{\bar{\Delta}}{\Delta x}=4\right)$	0.0726	0.0735	0.0655	0.0409	0.1442	0.1315	0.1293	0.0711
$C_{SM}\left(\frac{\bar{\Delta}}{\Delta x}=8\right)$	0.0742	0.0687	0.0579	0.0423	0.1232	0.1169	0.1138	0.0622
$C_{GR}\left(\frac{\bar{\Delta}}{\Delta x}=4\right)$	0.1372	0.1397	0.1346	0.1344	0.1284	0.1280	0.1275	0.1328
$C_{GR}\left(\frac{\bar{\Delta}}{\Delta x}=8\right)$	0.1254	0.1257	0.1193	0.1180	0.1115	0.1118	0.1112	0.1180
$C_{SS}\left(\frac{\hat{\Delta}}{\Delta}=1,\frac{\bar{\Delta}}{\Delta x}=4\right)$	1.3352	1.3293	1.2938	1.2954	1.1312	1.1048	1.0983	1.2388
$C_{SS}\left(\frac{\hat{\Delta}}{\Delta}=1,\frac{\bar{\Delta}}{\Delta x}=8\right)$	1.6891	1.6069	1.5399	1.5661	1.2920	1.2560	1.2448	1.4671
$C_{SS}\left(\frac{\hat{\Delta}}{\Delta}=2,\frac{\bar{\Delta}}{\Delta x}=4\right)$	0.4934	0.4904	0.4705	0.4676	0.3845	0.3685	0.3655	0.4426
$C_{SS}\left(\frac{\hat{\Delta}}{\Delta}=2,\frac{\bar{\Delta}}{\Delta x}=8\right)$	0.6998	0.6260	0.5770	0.5870	0.4469	0.4303	0.4243	0.5369

level). The YO coefficients range from 0.2137 to 0.2751, with the lower values for OH at the larger $\bar{\Delta}/\Delta x$, while the HN values show little filter-width dependence. At fixed $\bar{\Delta}/\Delta x$, the OHe600 coefficient lies between the HN and OH values, and is approximately equal to the average coefficient computed over all layers; this behavior was also observed for all the other models. Except for the SM model, where the trend is reversed, for a given $\bar{\Delta}/\Delta x$, the HN values are higher than the OH values. The range of coefficient values is 0.0409–0.1442 (SM), 0.1112-0.1397 (GR), 1.0988–1.6891 (SS1) and 0.3655–0.6998 (SS2). For the SM model, the coefficients are statistically independent of run and filter width, because the underlying the SM coefficients have a large spread of slopes (large standard deviation, e.g. Table 5 for OHe600). This result indicates that the correlation of the SM model with the SGS-fluxes is too poor for this calibration procedure to produce a meaningful coefficient.

For the GR and SS models, the statistical equivalence of the coefficients in Table 6 mirrors the closeness of numerical values, due to the small variation (small standard deviation) in the underlying slopes. For both models, the coefficients are filter-width dependent for each run. At either $\bar{\Delta}/\Delta x$, the three OH coefficients are (statistically) equal, the HN coefficients are also generally equal, and OHe600 is generally equal to the closest HN value (HN600 or HN800). For the GR model, the HN400 and HN500 values at $\bar{\Delta}/\Delta x = 8$ are equal to the OH values at $\bar{\Delta}/\Delta x = 4$. For the SS1 model, the HN values at $\bar{\Delta}/\Delta x = 4$ are equal to the OH750 value at $\bar{\Delta}/\Delta x = 8$. For the SS2 model, the OHe600 value at $\bar{\Delta}/\Delta x = 4$ is equal to the OH values at $\bar{\Delta}/\Delta x = 8$. Based on the $\bar{\Delta}/\Delta x$- and run-dependence of the GR coefficients, it is anticipated that dynamic modeling, wherein the model coefficient is computed during the LES from the LES flow field, will be required. Because dynamic modeling is based on the SS model with C_{SS}=1, the fact that the SS1 coefficient values are closer to unity than are the SS2 values suggests that $\hat{\Delta} = \bar{\Delta}$ has the greater potential for dynamic modeling. An *a posteriori* study is needed to determine the sensitivity of the LES to the model coefficients.

IV. Summary and conclusions

Large Eddy Simulation (LES) equations have been derived for compressible real-gas non-ideal-mixture flows, by applying a spatial filter to the Direct Numerical Simulation (DNS) equations. The LES equations

contain unclosed terms that cannot be computed directly from the filtered flow field, including the SGS fluxes that arise from filtering the convective terms. Using an existing DNS database of supercritical binary-species temporal mixing layer simulations, explicit models for the SGS fluxes and simplifying assumptions for the remaining unclosed terms were assessed *a priori*. The DNS database consists of transitional states of high pressure heptane/nitrogen, oxygen/hydrogen and oxygen/helium layers. The various assumptions were found to be valid, and the filtered thermodynamic quantities as well as the filtered viscous, species-mass and heat fluxes were found to be well-approximated by using the DNS functional form on the filtered flow field; the species-mass and heat fluxes contain Soret and Dufour effects, respectively. For modeling the SGS fluxes, constant-coefficient versions of Smagorinsky, Gradient and Similarity models were assessed and calibrated on the DNS database. The Smagorinsky model showed poor correlation with the exact SGS fluxes, while the Gradient and Similarity models had high correlations. Furthermore, the calibrated coefficients for the Gradient and Similarity models yielded good quantitative agreement with the SGS fluxes. However, comparison among the layers in the DNS database revealed that, statistically speaking, the calibrated coefficients were not generally valid. Future studies involve assessing the LES models *a posteriori* to determine their predictive ability in reproducing the temporal and spatial evolution of the filtered flow field, with particular interest on the sensitivity of the results to the value of the SGS-flux model coefficients.

V. Acknowledgments

This work was conducted at the Jet Propulsion Laboratory (JPL), California Institute of Technology (Caltech) and sponsored by the National Aeronautics and Space Administration (NASA) Fluid Microgravity Program under the direction of Dr. Walter Duval, by the Air Force Office of Scientific Research under the direction of Dr. Julian Tishkoff, and by the Army Research Office under the direction of Dr. David Mann, through interagency agreements with NASA. The computational resources were provided by the JPL Supercomputing Center. The authors would like to thank Dr. Kenneth Harstad of JPL for the transport property fits.

Appendix. Transport properties for O_2/He mixtures

For O_2/He mixtures, the Prandtl number is approximated as

$$\mathrm{Pr} = 0.68 + 0.0283\xi - 0.5017\xi^2 - 0.5390\xi^3 + \Delta\,\mathrm{Pr} \tag{40}$$

where

$$\xi = \min\left(0.5, Y_2 - 0.81\theta^{0.35}\right), \quad \theta = (T - 100)/800, \;\; 0 \le \theta \le 1, \; (T \text{ in Kelvin})$$

For $0.02 \le \theta \le 0.368$, $\Delta\,\mathrm{Pr} = 2.42 Y_2^{14.6} \max\left(0.0, -0.23\left(1 + \ln\theta\right)\right)$, otherwise $\Delta\,\mathrm{Pr} = 0$.

For O_2/He mixtures, the Schmidt number is approximated as

$$\begin{aligned} Sc &= \Sigma\left(Y_2\right)\left[1 + (114/T)^{1.5}\right]/\left(1 + \Delta_s\right) \\ T &< 200\text{K}: \; \Sigma = \left(1.292 - 0.757Y_2 + 0.444Y_2^2 - 0.757Y_2^3\right) \\ T &> 200\text{K}: \; \Sigma = \left(1.318 - 0.772Y_2 + 0.453Y_2^2 - 0.772Y_2^3\right) \end{aligned} \tag{41}$$

For p <30 MPa, $\Delta_s = \min\left(0.08, 0.1264 + 0.226Y_R\right) + 0.1\exp\left(-2400\theta^{4.5}\right)$ where $Y_R = Y_2 - \min\left(1, 0.5 + 0.78\theta^{0.6}\right)$, otherwise $\Delta_s = 0$.

References

[1]Prausnitz, J., Lichtenthaler, R., and de Azevedo, E., *Molecular Thermodynamics for Fluid-Phase Equilibrium*, Prentice-Hall, 1986.

[2]Hirshfelder, J., Curtis, C., and Bird, R., *Molecular Theory of Gases and Liquids*, John Wiley and Sons, 1964.

[3]Chehroudi, B., Talley, D., and Coy, E., "Initial Growth Rate and Visual Characteristics of a Round Jet into a Sub- to Supercritical Environment of Relevance to Rocket, Gas Turbine and Diesel Engines," AIAA 99-0206, 37th AIAA Aerospace Sciences Meeting Conference and Exhibit, January 11-14, 1999 ,Reno, NV.

[4]Mayer, W., Schik, A., Schweitzer, C., and Schaffler, M., "Injection and Mixing Processes in High Pressure LOX/GH2 Rocket Combustors," AIAA 96-2620, AIAA/ASME/SAE/ASEE 32nd Joint Propulsion Conference, July 1-3, 1996, Lake Buena Vista, FL.

[5]Mayer, W., Ivancic, B., Schik, A., and Hornung, U., "Propellant Atomization in LOX/GH2 Rocket Combustors," AIAA 98-3685, AIAA/ASME/SAE/ASEE 34th Joint Propulsion Conference and Exhibit, July 13-15,1998, Cleveland, OH.

[6]Oschwald, M. and Schik, A., "Supercritical Nitrogen Free Jet Investigated by Spontaneous Raman Scattering," *Experiments in Fluids*, Vol. 27, 1999, pp. 497–506.

[7]Miller, R., Harstad, K., and Bellan, J., "Direct Numerical Simulations of Supercritical Fluid Mixing Layers Applied to Heptane-Nitrogen," *Journal of Fluid Mechanics*, Vol. 436, 2001, pp. 1–39.

[8]Okong'o, N. and Bellan, J., "Direct Numerical Simulation of a Transitional Supercritical Binary Mixing Layer: Heptane and Nitrogen," *Journal of Fluid Mechanics*, Vol. 464, 2002, pp. 1–34.

[9]Okong'o, N. and Bellan, J., "Real Gas Effects of Mean Flow and Temporal Stability of Binary-Species Mixing Layers," *AIAA Journal*, Vol. 41, No. 12, December 2003, pp. 2429–2443.

[10]Okong'o, N. and Bellan, J., "Turbulence and Fluid-Front Area Production in Binary-Species, Supercritical, Transitional Mixing Layers," *Physics of Fluids*, Vol. 16, No. 5, May 2004, pp. 1467–1492.

[11]Keizer, J., *Statistical Thermodynamics of Nonequilibrium Processes*, Springler-Verlag, New York, 1987.

[12]Harstad, K. and Bellan, J., "An All-Pressure Fluid-Drop Model Applied to a Binary Mixture: Heptane in Nitrogen," *International Journal of Multiphase Flow*, Vol. 26, No. 10, 2000, pp. 1675–1706.

[13]Harstad, K. and Bellan, J., "Behavior of a Polydisperse Cluster of Interacting Drops Evaporating in an Inviscid Vortex," *International Journal of Multiphase Flow*, Vol. 23, No. 5, 1997, pp. 899–925.

[14]Okong'o, N., Harstad, K., and Bellan, J., "Direct Numerical Simulations of O_2/H_2 Temporal Mixing Layers Under Supercritical Conditions," *AIAA Journal*, Vol. 40, No. 5, May 2002, pp. 914–926.

[15]Harstad, K. and Bellan, J., "Isolated Fluid Oxygen Drop Behavior in Fluid Hydrogen at Rocket Chamber Pressures," *International Journal of Heat and Mass Transfer*, Vol. 41, 1998, pp. 3537–3550.

[16]Papamoschou, D. and Roshko, A., "The Compressible Turbulent Shear Layer: An Experimental Study," *Journal of Fluid Mechanics*, Vol. 197, 1988, pp. 453–477.

[17]Moser, R. and Rogers, M., "Mixing Transition and the Cascade to Small Scales in a Plane Mixing Layer," *Physics of Fluids A*, Vol. 3, No. 5, 1991, pp. 1128–1134.

[18]Moser, R. and Rogers, M., "The Three-Dimensional Evolution of a Plane Mixing Layer: Pairing and Transition to Turbulence," *Journal of Fluid Mechanics*, Vol. 247, 1993, pp. 275–320.

[19]Okong'o, N. and Bellan, J., "Consistent Boundary Conditions for Multicomponent Real Gas Mixtures Based on Characteristic Waves," *Journal of Computational Physics*, Vol. 176, 2002, pp. 330–344.

[20]Kennedy, C. and Carpenter, M., "Several New Numerical Methods for Compressible Shear Layer Simulations," *Applied Numerical Mathematics*, Vol. 14, 1994, pp. 397–433.

[21]Muller, S. M. and Scheerer, D., "A Method to Parallelize Tridiagonal Solvers," *Parallel Computing*, Vol. 17, 1991, pp. 181–188.

[22]Okong'o, N. and Bellan, J., "Consistent Large Eddy Simulation of a Temporal Mixing Layer Laden with Evaporating Drops. Part 1: Direct Numerical Simulation, Formulation and *A Priori* Analysis," *Journal of Fluid Mechanics*, Vol. 499, 2004, pp. 1–47.

[23]Leboissetier, A., Okong'o, N., and Bellan, J., "Consistent Large-Eddy Simulation of a Temporal Mixing Layer Laden with Evaporating Drops. Part 2: *A Posteriori Modeling*," *Accepted, Journal of Fluid Mechanics*, 2004.

[24]Smagorinksy, J., "Some Historical Remarks on the Use of Nonlinear Viscosities," *Large Eddy Simulation of Complex Engineering and Geophysical Flows*, edited by B. Galperin and S. Orszag, chap. 1, Cambridge University Press, 1993, pp. 3–36.

[25]Yoshizawa, A., "Statistical Theory for Compressible Turbulent Shear Flows, With the Application to Subgrid Modeling," *Physics of Fluids*, Vol. 29, No. 7, 1986, pp. 2152–2164.

[26]Clark, R., Ferziger, J., and Reynolds, W., "Evaluation of Subgrid-Scale Models Using an Accurately Simulated Turbulent Flow," *Journal of Fluid Mechanics*, Vol. 91, No. 1, 1979, pp. 1–16.

[27]Bardina, J., Ferziger, J., and Reynolds, W., "Improved Subgrid Scale Models for Large Eddy Simulation," AIAA 80-1357, 1980.

[28]Liu, S., Meneveau, C., and Katz, J., "On the Properties of Similarity Subgrid-Scale Models as Deduced from Measurements in a Turbulent Jet," *Journal of Fluid Mechanics*, Vol. 275, 1994, pp. 83–119.

[29]Pruett, C., Sochacki, J., and Adams, N., "On Taylor-Series Expansions of Residual Stress," *Physics of Fluids*, Vol. 13, No. 9, September 2001, pp. 2578–2589.

[30]Harstad, K. and Bellan, J., "The D^2 Variation For Isolated LOX Drops and Polydisperse Clusters in Hydrogen at High Temperature and Pressures," *Combustion and Flame*, Vol. 124, No. 4, 2001, pp. 535–550.